Effects of particle density and fluid properties on mono-dispersed granular flows in a rotating drum

Yu Chen ; Si Suo ; Mingrui Dong ; Haiyi Zhong; Deheng Wei ; Yixiang Gan

Check for updates

View Online Export Citation

Articles You May Be Interested In

Transforming underground to surface mining operation – A geotechnical perspective from case study

AIP Conference Proceedings (November 2021)

Monthly prediction of rainfall in nickel mine area with artificial neural network

AIP Conference Proceedings (November 2021)

Estimation of Karts groundwater based on geophysical methods in the Monggol Village, Saptosari District, Gunungkidul Regency

AIP Conference Proceedings (November 2021)

Physics of Fluids

Special Topic:

Flow Engineering with Smart Interfaces

Guest Editors: Xu Chu and Guang Yang

Submit Today!

AIP Publishing

Effects of particle density and fluid properties on mono-dispersed granular flows in a rotating drum

View Online   Export Citation   CrossMark

Yu Chen,[1] ⓘ Si Suo,[2,a)] ⓘ Mingrui Dong,[1] ⓘ Haiyi Zhong,[1] Deheng Wei,[1,3] ⓘ and Yixiang Gan[1,a)] ⓘ

AFFILIATIONS

[1]School of Civil Engineering, The University of Sydney, Camperdown, NSW 2006, Australia
[2]Department of Civil and Environmental Engineering, Imperial College London, London SW7 2AZ, United Kingdom
[3]Key Laboratory of Ministry of Education on Safe Mining of Deep Mines, School of Resources and Civil Engineering,
 Northeastern University, Shenyang, China

[a)]Authors to whom correspondence should be addressed: s.suo@imperial.ac.uk and yixiang.gan@sydney.edu.au

ABSTRACT

Due to their simple geometric configuration and involved rich physics, rotating drums have been widely used to elaborate granular flow dynamics, which is of significant importance in many scientific and engineering applications. This study both numerically and experimentally investigates dry and wet mono-dispersed granular flows in a rotating drum, concentrating on the effects of relative densities, $\rho_s - \rho_f$, and rotating speeds, ω. In our numerical model, a continuum approach based on the two-phase flow and $\mu(I)$ theory is adopted, with all material parameters calibrated from experimental measurements. It is found that, in the rolling and cascading regimes, the dynamic angle of repose and the flow region depth are linearly correlated with the modified Froude number, Fr^*, introducing the relative density. At the pore scale, flow mobility can be characterized by the excess pore pressure, p_f. To quantify the variance of the local p_f, it is specifically non-dimensionalized as a pore pressure number, K, and then manifested as a function of porosity, $1 - \phi_s$. We find $K(\phi_s)$ approximately follow the same manner as the Kozeny–Carman equation, $K \propto \phi_s{}^2/(1 - \phi_s)^3$. Furthermore, we present the applicability of the length-scale-based rheology model developed by Ge *et al.* ["Unifying length-scale-based rheology of dense suspensions," Phys. Rev. Fluids **9**, L012302 (2024)], which combines all the related time scales in one dimensionless number G, and a power law between G and $1 - \phi_s/\phi_c$ is confirmed. This work sheds new lights not only on the rigidity of implementing continuum simulations for two-phase granular flows, but also on optimizing rotating drums related engineering applications and understanding their underlying mechanisms.

I. INTRODUCTION

Granular materials, composed of discrete solid particles, are commonly dispersed in ambient fluids. This combination driven by gravity is common in nature, e.g., snow avalanches,[1,2] sand-fall landslides,[3,4] debris flows,[5–7] and in various industrial applications, e.g., drying, mixing, and segregation processes.[8–10] Understanding and predicting the behavior of granular flow is thus crucial. The granular flow depends on particle characteristics, such as size, shape, and density,[11–13] as well as the properties of ambient fluids.[14–16] The ambient fluid within porous granular media is typically air or water. Unlike dry granular flows extensively studied over recent decades,[17–20] wet granular flows present significant challenges due to the complex interactions between the particles and the ambient fluids.[21–23] As a simple, yet effective tool to study these complex phenomena, such as disorder, pattern formation, threshold dynamics, segregation, etc., the rotating drum has

contributed to analyzing the underlying dynamics of the granular flows.[24–26] In addition to its wide applications to scientific research, including solitary waves,[27] segregation in dilute suspensions,[28] avalanches in granular matter,[29] and many others,[30] the rotating drum is also used in different engineering processes, such as mixing in the pharmaceutical industry[31–33] and wood debarking in the pulp and paper industry.[34] However, the rich physics involved in rotating drums, when the heavy fluid comes into play, are seldom isolated to be studied; in particular, how the relative density between the particles and the fluid affects granular flow behavior deserves more attempts.

Wet granular flow can be considerably complex by the existence of a viscous pore fluid. Being comprised of macroscopically large grains, cohesion between particles—arising from surface forces such as liquid bridges—is mostly disregarded.[35] These forces, rooted in the contact area, can be considered negligible for large hard particles with

04 October 2024 23:02:14

low ratios of contact area to volume.[36,37] When solid particles are submerged in an ambient fluid with low density and viscosity, such as glass beads in air, the influence of the fluid dynamic properties on granular flow can generally be ignored.[15,38] In this condition, the behavior of the granular flow is significantly dominated by particle–particle interactions and gravitational forces directly related to the particle bulk density.[39–42] However, it is more complex when the density of the ambient fluid is comparable to that of the solid cases. The buoyancy parameter $[\Delta\rho/\rho_s = (\rho_s - \rho_f)/\rho_s]$, dependent on the densities of particle, ρ_s, and fluid, ρ_f, is proposed to indicate the impact of density discrepancies on flow dynamics, leading to distinct behavior from dry granular flow.[43–45] In particular, Jain et al.[46] found the basic characteristics of granular flow involving large and heavy beads in a rotating drum remain consistent, even when the drum is filled with heavy fluid. Cassar et al.[47] demonstrated that different flow regimes of dry and wet cohesionless granular materials can be characterized by the Stokes number and the grain-fluid density ratio in uniform flows along inclined channels. Liao et al.[48] experimentally analyzed the effective density ratio effects on the granular streak segregation behavior. In fact, the interaction between the fluid and granular phase is essentially dependent on the fluid pressure, also called pore pressure, influencing the effective friction force acting on the granular medium.[38,42,49] Solid–fluid mixture flows are categorized into two types based on the dominant driving forces: (i) grain-inertial flows, where solid particle collisions are the primary mechanism for momentum exchange, and (ii) macro-viscous flows, where the forces on grains are mainly from the viscosity of pore fluid.[50] In grain-inertial flows, the momentum transfer is driven by the velocity differences between adjacent layers of particles, generating stresses proportional to the square of the shear rate. Conversely, in macro-viscous flows, it is the resistance due to the viscosity of fluid that governs the flow dynamics.[47,51]

Solid–liquid mixture experiments, i.e., chute flow, column collapse, and rotating drums, have provided insights into the dynamics of granular flows. The chute flow experiments underscore the significance of fluid viscosity in shaping granular flow thickness and velocity profiles.[52,53] Further explorations in controlled granular column collapse experiments[54–57] highlight the role of grain size, pore fluid, and initial packing states in granular dynamics; the studies collectively show that the grain mobility such as runout distances, final heights, and duration of collapse. Recent studies in rotating drum experiments reveal that pore fluid properties and processing parameters, such as the volume and viscosity of fluids,[14,58,59] baffle configurations,[60–62] rotating speeds,[58,63] filling rate,[64,65] and sidewall effect,[66–68] significantly influence the granular flow dynamics. Previous theoretical models for granular flows have successfully captured granular flow morphology and velocity, and pressure fields within it.[42,63,69] The commonly employed kinetic theory[23,70–74] of granular flow is limited to addressing dense granular flows, especially near packing limits where high pressure and density could cause more particle interactions. Applying this theory to submerged granular flow shows inadequacy in the fluid pressure fields of dense samples. The recently developed $\mu(I)$ rheology model offers a more solid framework, effectively capturing the transition between different flow regimes across the solid-like, liquid-like, and gas-like regimes. Jop et al.[75] proposed a constitutive model for granular flows in the liquid-like regime, successfully capturing the correspondingly essential features, such as the yield criterion and how viscosity changes with different deformation rates and internal stresses. In parallel, Lee[69]

advanced the $\mu(I)$ theory, characterizing shear-induced volumetric changes and the consequent pore pressure dynamics in submerged granular flows. Recently, an alternative, scale-based rheology model is proposed for the representation of dense suspension flows.[76–78] Such an enhanced model provides a deeper understanding of the behavior of granular materials within ambient fluid. In addition, the rheological properties μ_s and μ_d, which characterize the frictional and viscous behavior of granular flow, are influenced by the properties of the solid particles in size and density. Based on the measured values of these parameters in Pouliquen's[17] that are specialized for glass beads of various sizes, subsequent studies[38,79,80] have applied these values in numerical simulations dedicated to scenarios with glass beads involved in. However, whether this approach is appropriate to other systems than being composed of glass beads needs to be clarified; if yes, how the specific values of μ_s and μ_d are influenced by particle properties should also be quantified.

To gain deep insight into the complicated interaction between granular flow and ambient fluid, of which the detailed micro information is difficult to be measured experimentally, the commonly adopted numerical approaches are based on the discrete element method (DEM),[21,81,82] coupled computational fluid dynamics and DEM (CFD-DEM),[83–88] and coupled smooth particle hydrodynamics and DEM (SPH-DEM).[89–91] The treatment of particle–fluid interactions in the CFD-DEM resolves the pore-scale fluid flow inside pores of particle assemblies. The fully resolved scheme for the CFD-DEM directly calculates the particle–fluid interaction forces via the integration of the fluid stress over the surface of the particle.[92,93] Another un-resolved scheme proposed by Tsuji et al.[94] solved the particle–fluid interactions at a locally averaging scale, where fluid flow inside the pores of particle assembly is not resolved. However, these DEM-based frameworks are limited to employ large amounts of particles due to their high computation cost requirements, and the extensive calibration of particle-scale parameters is complexity. While CFD-DEM can be a more accurate method capturing individual particle dynamics, the number of modeling parameters is significantly higher.[95,96] These parameters are not necessarily measurable from experiments and often require extensive calibrations. In contrast, the two-fluid method (Eulerian–Eulerian) based on computational fluid dynamics (CFD) offers a viable alternative. The approach treats both solid and fluid phases as continuous, yet interpenetrating media, thus enabling the involvement of essential interactions between them in a more computationally efficient fashion.[23,97] Recent years have witnessed considerable progress in delineating the transition of submerged granular flows from viscous to inertial regimes. This advancement is crucial in effectively predicting the pore pressure dynamics within these systems.[38,42]

The laboratory-scale rotating drum test effectively replicates the granular avalanche phenomenon in field.[98] As the rotation speed increases, individual avalanches become indistinguishable, leading to the onset of continuous flow regimes. The granular flows in a rotating drum are typically characterized by a moving surface layer over a densely packed, relatively static bed that moves as a solid mass, remaining stationary compared to the rotation of the drum.[99] With the increase in the rotating speed, seven different flow regimes can be observed: sliding, surging, slumping, rolling, cascading, cataracting, and centrifuging. Rajchenbach[100] experimentally investigated the transition between discrete avalanches and continuous flow, reporting a hysteretic nature of the transition and a square root dependence of the

dynamic angle of repose, θ_m, on the rotation rate, ω. Further experimental[101,102] and numerical studies,[103,104] however, found a linear relationship between θ_m and ω. According to the forms of transverse bed motion, the first two are typically slipping motions. Such types of motion are of no clearly practical applications, neither are the last two of high rotating speed.[105,106] Under the conditions of median rotating speed, the mixing process of rotating grains has sufficient engineering applications, such as rotary kilns and reactors, rotary dryers and coolers, and mixing drums. As stressed in many studies, the rolling regime is distinguished by its steady-state circulation between the upper fluid-like flow and the lower solid-like plug flow, marked by an inclined and straight free surface. In contrast, cascading flows introduce a gas-like regime characterized by swift, dilute flows with particle interactions predominantly through collisions.[107–110] Theoretical studies of the flowing layer employed simplified assumptions, grounded in continuum models. Zik et al.[111] modeled the flowing layer as a thin, viscous fluid of uniform height, assuming the flow was tangential to the free surface and that the density remained constant; the free surface is reproduced by balancing the stresses within the layer. Khakhar et al.[112] investigated both the flow within the free surface and grain mixing, incorporating mass flux and an explicit viscosity expression based on Bagnold's work[50] on non-dilute sheared suspensions. They examined three flow scenarios—plug flow, Bagnold's profile, and simple shear—finding that the latter two closely matched experimental observations for glass spheres in terms of average velocity and layer thickness.

A dimensionless parameter—the Froude number—defined as the ratio of the inertial forces to the gravitational forces, $Fr = \sqrt{\omega^2 R/g}$,[21,113] where ω is the rotating speed, R the drum radius, and g the gravitational acceleration, is traditionally applied to the dry flows in rotating drums.[73,114,115] Meanwhile, to account for buoyancy in an ambient liquid granular system, a modified Froude number, $Fr = \sqrt{\rho_s \omega^2 R/\Delta\rho g}$, has been proposed to the submerged granular systems.[16,43] The dynamic angle of repose, θ, observed at the surface of the flowing layer and indicative of inter-particle friction, increases linearly with Froude number.[16,73,116] Furthermore, the normalized active flowing layer depth (h) by the mean grain size (d), h/d, scales exponentially with the shear rate, $v/\sqrt{gd^3}$, inside the drum,[16,117,118] thereby providing additional insight into the pattern transitions.

While introducing Froude number helps distinguish flow patterns, there remains a gap in apprehending its applicability across different granular flow scenarios incorporating buoyancy and viscous effects from the pore fluid. Furthermore, the variations in buoyancy parameter and their impact on flow dynamics point to a research gap in the field of granular rheology. Finally, compared with dry conditions, how pore pressure distribution within submerged granular flow is influenced by packing fraction remains scarcely investigated. To bridge these gaps, this study aims to numerically and experimentally discuss the effects of properties of both particles and pore fluids on the dynamics of granular flow in a rotating drum; the focus is on the detailed comparison between dry and submerged conditions. We finally propose a practical scaling relationship covering a wide range of parameter space. The findings of this study not only contribute to a deeper understanding of granular flow dynamics in rotating drum systems under varying conditions of buoyancy, viscosity, and pressure distribution but also provide valuable insights for designing and optimizing processes involving granular materials, such as industrial mixing and sediment transportation.

II. METHODOLOGY

In this section, we introduce the employed experimental setups and numerical simulation methods. Main attention is paid to rolling and cascading regimes due to their sought-after scientific and engineering applications. The implemented grains are mono-sized spheres made of polyoxymethylene, glass beads, or stainless steel, while the fluid liquid is deaired water. Moreover, our numerical method is based on a two-phase flow CFD, which provides the detailed insights into fluid and solid pressure within the granular flow.

A. Experimental setup and procedure

The experiment apparatus used in this work is illustrated in Fig. 1(a). Experiments are performed under both dry and submerged conditions. In the dry condition, particles are loaded directly into the drum in air and secured with screws. For the submerged condition, the initial particle filling and drum assembly are conducted in a fully immersed water tank to ensure the absence of air bubbles. Following each experiment, the particles are removed and reloaded using a consistent method to maintain uniformity across all trials. For the convenience of direct observation and measurement, the cylindrical drum and two end plates are fabricated transparent acrylic. The drum is 75 mm in inner radius and 30 mm in axial length. To prevent water leakage, the gap between drum and sidewall is well sealed using water-proof strips. In the motorized stage, a range of rotating speed, ω, from 5 to 60 rpm, is utilized for the need of the rolling and cascading regimes of prior interest in this study. For each trial, a constant rotational speed is maintained, and particle motion is recorded using a high-speed camera. This allows for precise capture of the dynamic angle of repose. To ensure the repeatability of the results, individual data points in experiments are performed with five repetitions, and the maximum standard deviation of measured values is less than 5%. This indicates that the data have a good repetition and are reliable for the following analysis. Table I shows our experimental repeatability across all materials and rotating speed, by averaging five repeated experiments. To capture the movements of continuous granular flow especially at a high rotating speed, a high-speed camera with 1000 fps and the resolution of 1920×1080 pixels (0.2 mm/pixel) was employed to record rotating processes. Combined with the particle image velocimetry (PIV) analysis,[119] the velocity field of the granular flow is reconstructed, and local shear rate and flow mode are correspondingly calculated and determined. More details regarding the setup can be found in Table II.

We adopt three types of particles as shown in Fig. 1(a): polyoxymethylene (POM, $\rho_s = 1382\,\text{kg/m}^3$), glass beads ($\rho_s = 2363\,\text{kg/m}^3$), and stainless steel ($\rho_s = 7803\,\text{kg/m}^3$), with the same diameter of 2 mm ± 3%. We have confirmed that such a narrow range of grain size distribution could not induce much crystallization in the rotated grains under the weak stress state. The initial packing fractions for all types of grains are approximately 61.8%; the total mass of polyoxymethylene, glass beads, and stainless-steel spheres is about 114.50, 195.77, and 646.48 g, respectively. The submerged conditions correspond to the case where grains are rotated in the water. The laboratory temperature and ambient pressure are maintained at 22 °C and 1 atm, respectively.
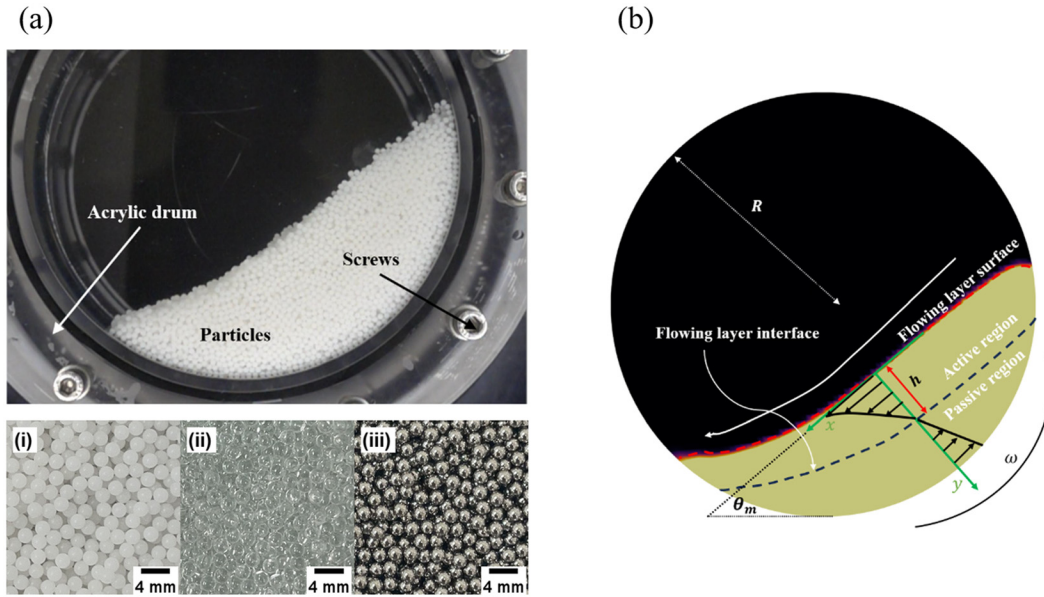
FIG. 1. (a) A snapshot of the rotating drum experiments containing polyoxymethylene particles under submerged conditions with $\omega = 10$ rpm, under which are particles used in experiments: (i) polyoxymethylene, (ii) glass beads, and (iii) stainless steel. (b) Corresponding simulation results to the experiment in (a). The drum radius is denoted by $R = 75$ mm, and the dynamic angle of repose and maximum flow region depth are represented by θ and h, respectively.

TABLE I. Measurement of average angle of repose in repeatable experiments.

		5 rpm	10 rpm	20 rpm
POM	Dry	$32.3° \pm 2.0\%$	$35.2° \pm 1.8\%$	$41.3° \pm 1.6\%$
	Submerged	$34.4° \pm 3.1\%$	$40.7° \pm 3.2\%$	$49.9° \pm 3.4\%$
Glass	Dry	$31.3° \pm 3.9\%$	$33.7° \pm 3.8\%$	$39.1° \pm 3.2\%$
	Submerged	$31.0° \pm 3.5\%$	$36.0° \pm 3.2\%$	$42.6° \pm 3.5\%$
Steel	Dry	$28.6° \pm 2.7\%$	$30.8° \pm 2.5\%$	$35.9° \pm 3.1\%$
	Submerged	$26.9° \pm 4.6\%$	$30.4° \pm 4.1\%$	$35.6° \pm 4.5\%$

TABLE II. Details of experimental equipment.

Equipment	Model	Accuracy/specification
Motorized stage	01SC403 Stepping Motor Controllers	$\pm 0.001\,38$ rpm
Drum	Acrylic Fabrication	Inner radius:75 mm; axial length: 30 mm
High-speed camera	Sony DSC-RX100	1920×1080 pixels, ≤ 1000 fps
Strip	Rubber O-ring	Waterproof; outer radius: 78 mm

B. Numerical simulation

The numerical model is conducted through coupling a two-phase flow framework and $\mu(I)$ rheology model. The two-phase flow framework considers the granular phase as an effective "fluid" phase, with special treatments for interactions between pore fluids and granular materials. We incorporate the $\mu(I)$ theory in the "twoPhaseEulerFoam" solver based on OpenFOAM-9. The PIMPLE algorithm combines the pressure-implicit split-operator (PISO) and the semi-implicit method for pressure-linked equations (SIMPLE) algorithms.[120]

A circular domain, as shown in Fig. 1(b), is adopted, and its geometry follows the experiment setup. The mesh size for the simulations is carefully determined through a mesh-size sensitivity study, wherein three mesh sizes, ℓ, with $\ell/R = 1/15$, $1/37.5$, and $1/75$, are taken into consideration. The mesh independence test in Fig. 2, in terms of the angle of repose, is measured to be $29.8°$, $30.4°$, and $30.4°$, respectively; it indicates the mesh refinement to $\ell/R = 1/75$, leading to minimal changes, and thus, the convergency of results is achieved at $\ell/R = 1/35$. The number of observations refers to the measurement of the dynamic angle of repose at various time steps, when the granular flow reaches the steady-state condition. The corresponding grain flow morphology is also well validated against experimental results. Ultimately, the $\ell/R = 1/37.5$ mesh size is selected for our numerical simulations due to its lower computational cost while still maintaining accurate results. The domain is first meshed using uniform hex cell with $1/37.5$ in length; based on this background mesh, the circular boundary is adapted and refined to a size ranging from $1/75$ to $1/37.5$. The time step is determined by the given maximum Courant number $C_{o,\max}$, and the sensitive study indicates $C_{o,\max} = 0.8$ can guarantee a convergent result.

1. Governing equations

The two-phase flow is modeled based on the Eulerian–Eulerian framework in which fluid and particle dynamics are described using
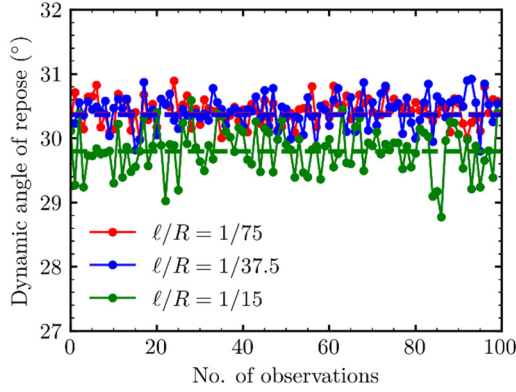
FIG. 2. Grid sensitivity study with varying mesh sizes at 5 rpm for dry granular flow of glass beads.

the Eulerian scheme. The mass and momentum equations for the fluid phase are expressed as

$$\frac{\partial \phi_f}{\partial t} + \nabla \cdot (\phi_f \boldsymbol{U}_f) = 0 \tag{1}$$

and

$$\rho_f \left[\frac{\partial \phi_f \boldsymbol{U}_f}{\partial t} + \nabla \cdot (\phi_f \boldsymbol{U}_f \cdot \boldsymbol{U}_f) \right] = -\phi_f \nabla p_f + \nabla (\phi_f \boldsymbol{\tau}_f) + \rho_f \phi_f \boldsymbol{g} - \boldsymbol{F}_d; \tag{2}$$

for the particle phase, they read as

$$\frac{\partial \phi_s}{\partial t} + \nabla \cdot (\phi_s \boldsymbol{U}_s) = 0 \tag{3}$$

and

$$\rho_s \left[\frac{\partial \phi_s \boldsymbol{U}_s}{\partial t} + \nabla \cdot (\phi_s \boldsymbol{U}_s \cdot \boldsymbol{U}_s) \right] = -\phi_s \nabla p_f - \nabla (\phi_s p_s)$$
$$+ \nabla (\phi_s \boldsymbol{\tau}_s) + \rho_s \phi_s \boldsymbol{g} + \boldsymbol{F}_d. \tag{4}$$

The subscripts f and s indicate the fluid and particle phase, respectively; ρ is the density, $\boldsymbol{U}$ the velocity vector, p the pressure, $\boldsymbol{g}$ the gravitational acceleration, $\boldsymbol{\tau}$ the shear stress, and $\boldsymbol{F}_d$ the fluid–particle interaction force. ϕ is the phase volume fraction[23] and satisfies

$$\phi_f + \phi_s = 1. \tag{5}$$

Two pore fluids are considered, i.e., air ($\rho_{f,a} = 1.29 \text{ kg/m}^3$, $\eta_{f,a} = 1.81 \times 10^{-5} \text{ Pa s}$) and water ($\rho_{f,w} = 993 \text{ kg/m}^3$, $\eta_{f,w} = 1 \times 10^{-3} \text{ Pa s}$), where η_f is the dynamic shear viscosity and subscripts a and w denote the air and water, respectively. The viscous stress tensor for the fluid phase and solid phase has the following form:

$$\begin{cases} \boldsymbol{\tau}_f = \eta_f \left(\nabla \boldsymbol{U}_f + (\nabla \boldsymbol{U}_f)^T - \frac{2}{3}(\nabla \cdot \boldsymbol{U}_f)\boldsymbol{I} \right), \\ \boldsymbol{\tau}_s = \eta_s \left(\nabla \boldsymbol{U}_s + (\nabla \boldsymbol{U}_s)^T - \frac{2}{3}(\nabla \cdot \boldsymbol{U}_s)\boldsymbol{I} \right), \end{cases} \tag{6}$$

where $\boldsymbol{I}$ is the unity tensor.

2. Phase interaction

The phase interaction originates from the relative motion of particles and ambient fluids, which is composed of the buoyance force, $\phi_f \nabla p_f$, and the interphase body force, F_d. F_d consists of drag force, virtual mass force, and lift force. Virtual mass force for the inertial component is negligible in this study with air or water fluid of low density involved in, which has been proved in our numerical framework; the identical flow patterns are encountered for simulations of POM-water flow with or without added mass force into considerations. Lift force is also neglected due to the low Reynolds number and spherically shaped grains. According to Eqs. (7)–(10), the magnitude of F_d can be quantified by the Reynolds number. The lift force is expressed as $F_l = C_L \rho_f \left(\frac{\eta_f}{\rho_f} \right)^{0.5} d_s^2 (\boldsymbol{U}_f - \boldsymbol{U}_s) \left(\frac{d\boldsymbol{U}_f}{dy} \right)^{0.5}$, with the value of lift coefficient $C_L = 0.5$,[121] and the virtual mass force is represented as $F_{vm} = \frac{1}{6}\pi C_{vm} \rho_f d_s^3 \left(\frac{d\boldsymbol{U}_f}{dt} - \frac{d\boldsymbol{U}_s}{dt} \right)$, with the value of virtual mass coefficient C_{vm} of 0.5.[122] In our study, we did not include these two forces in our two-phase flow model, due to the magnitudes of $F_l/F_d \sim \mathcal{O}(10^{-10})$ and $F_{vm}/F_d \sim \mathcal{O}(10^{-9})$, which are neglectable compared to drag force. The drag force is dominant in fluid–grain interactions and strongly dependent on the relative speed between solid and fluid phases, $\boldsymbol{U}_f - \boldsymbol{U}_s$, fluid viscosity, grain size distribution, and void ratio,

$$\text{F}_d = \beta(\boldsymbol{U}_f - \boldsymbol{U}_s), \tag{7}$$

where β is the generalized drag coefficient. The formula developed by Gidspow[123] is adopted,

$$\beta = \begin{cases} \frac{3}{4} C_d \frac{Re_s}{d_s^2} \eta_f \rho_f \phi_s (1 - \phi_s)^{-1.65} & \text{if } \phi_s \leq 0.2, \\ \frac{150\phi_s^2 \eta_f}{(1-\phi_s)^2 d_s^2} + \frac{1.75\eta_f Re_s}{d_s^2} & \text{if } \phi_s > 0.2, \end{cases} \tag{8}$$

where C_d is the drag coefficient for a single particle, η_f fluid viscosity, and d_s the particle diameter. Re_s is the particle Reynold number and defined as

$$Re_s = \frac{\rho_f |\boldsymbol{U}_f - \boldsymbol{U}_s| d_s}{\eta_f}, \tag{9}$$

which also depends on C_d of spherical grains,

$$C_d = \begin{cases} \frac{24}{Re_s} \left(1 + 0.15 Re_s^{0.687}\right) & \text{if } Re_s < 1000, \\ 0.44 & \text{if } Re_s \geq 1000. \end{cases} \tag{10}$$

3. Granular stress and rheology

The internal pressure of the particle phase is determined by considering the normal and tangential behaviors of inter-particle contacts and calculated as

$$p_s = \begin{cases} 0, & \phi_s < \phi_{s,\min}^{Fric} \\ \text{Er} \frac{\left(\phi_s - \phi_{s,\min}^{Fric}\right)^{\eta_0}}{\left(\phi_{s,\max} - \phi_s\right)^{\eta_1}}, & \phi_s \geq \phi_{s,\min}^{Fric}, \end{cases} \tag{11}$$

where $\phi_{s,\min}^{\mathrm{Fric}} = 0.57$ and $\phi_{s,\max} = 0.635$ are, respectively the minimum and maximum volume fractions for random dense packing of mono-sized spheres,[69] and $E_r = 0.05\,\mathrm{GPa}$, $\eta_0 = 3$, and $\eta_1 = 5$ are empirical coefficients.[23] To determine the shear stress (τ_s) in the solid phase, an effective rheology model proposed by Jop *et al.*[75] is adopted. In this model, the apparent viscosity $\mu(I)$ is determined by the inertial number,

$$I = \frac{\dot{\gamma} d_s}{\sqrt{p_s/\rho_s}},\tag{12}$$

where $\dot{\gamma}$ is the shear rate, derived from the rate of velocity decrement,

$$\dot{\gamma} = \frac{1}{2}\left(\frac{\partial U_x}{\partial y} + \frac{\partial U_y}{\partial x}\right),\tag{13}$$

and ρ_s particle density, and $\mu(I)$ is in the form of

$$\mu(I) = \mu_s + \frac{\mu_d - \mu_s}{I_0/I + 1},\tag{14}$$

where I_0 is determined empirically and serves as a reference value, with smaller values of I indicating quasi-static behavior and larger values indicating rapid, fluid-like behavior, and μ_s and μ_d represent the static and dynamic friction coefficients, respectively.

The rheology model requires the determination of μ_s and μ_d. In this work, we measure μ_s and μ_d using an experimental fashion in dry flows. These values are used in the following numerical simulations for both dry and wet conditions. μ_d quantifies the resistance at the onset of granular motion inside the rotating drum and can be characterized by the "start angle," θ_{start}.[124] Specifically, we begin with the test when grains are at rest and then rotate the drum with an extremely slow rate until they just begin to flow. The inclination angle at this point, when particle movement initiates, is defined as θ_{start} and accordingly $\mu_d = \tan\theta_{\mathrm{start}}$.

μ_s is the static friction coefficient, characterizing the frictional resistance encountered once they are active in motion. This coefficient relates closely to the "stop angle," θ_{stop}, which represents the inclination angle at which the moving particles come to a halt.[125] Notably, $\mu_s < \mu_d$ always holds, suggesting that a smaller force is required to sustain particle motion compared with initiating it, contrary to the common sense, whereas the static friction coefficient is higher than dynamic friction coefficient for the same contact interface. In addition, θ_{stop} is measured as the inclination angle after the landslide in the drum has restored the pile to an equilibrium slope, and $\mu_s = \tan\theta_{\mathrm{stop}}$.

With the input parameters in hand, the boundary conditions are set as follows. The drum is rotated with the specified angular velocity, ω. The fluid moves at the same speed as the drum wall. Additionally, a zero-gradient boundary condition is imposed for the volume fraction and pressure field.

III. RESULTS

A. Experimental results

Our measurements of granular flow in the experiments include shear rate profiles, dynamic angles of repose, and flow depths; two flow regimes, i.e., rolling and cascading, are also identified. Furthermore, we propose a dimensionless number to relate the interface morphology to ρ_s, ρ_f, and ω.

1. Flow patterns

The flow patterns can be distinguished by the surface morphology.[106] When the surface is flat, i.e., the angle of repose remains constant, the flow is at the rolling regime; once the surface exhibits S-shape, i.e., angle of repose varies along the surface, the flow is at the cascading regime. As depicted in Fig. 3(a) for the dry condition, for all three types of particles, the systems exhibit the rolling regimes at 5 rpm; at 10 and 20 rpm, the system transitions to the cascading regime, with the surface becoming curved and the height of the arch increasing with ω. In Fig. 3(b) for the submerged condition, POM particles consistently show a cascading tendency from 5 to 20 rpm. However, for glass beads and stainless-steel particles, the systems remain in the rolling regime at 5 rpm and transitions to cascading at 10 and 20 rpm. It is revealed that the transition from rolling to cascading for higher-density particles requires a higher ω, due to the enhanced inertia and the increased gravitational pull. The comparative analysis between dry and submerged condition indicates that the viscosity and density of ambient fluid are also dominant in the flow patterns due to the drag force.

2. Shear rate

Understanding the flow field, particularly the velocity field, within a rotating drum is fundamentally important for a wide range of scientific and engineering applications. In traditional PIV analysis, just velocity fields[72,80,126] in a rotating drum are depicted without deeper insights into the shear rate distribution. In this study, we focus on the shear rate distribution for more effectively analyzing granular flow. Having shear rate at every point with an interval of 0.1 s, the shear rate profile is visualized using a contour plot representing the averaged local shear rates, as shown in Fig. 3. Different shear rate profiles are distinguished by particle type and rotating speed. Via this manifestation, we can characterize the local particle movement mechanisms in experiments.

Our experimental findings indicate that increasing rotating speed leads to a higher shear rate for all tested materials under both dry and submerged conditions. As the rotating speed increases, more kinetic energy is applied into the system, facilitating more intensive interparticle contacts and relative movements. This results in an enhancement of the shear rate due to the increased energy dissipation. In addition, higher particle densities influence the shear rates similarly.

Comparing dry conditions [Fig. 3(a)] with submerged conditions [Fig. 3(b)] reveals notable differences in the shear rates. In submerged cases, the shear rates are higher than those in dry cases. In dry conditions, the shear interactions are primarily governed by direct collisions between particles. Without the influence of a fluid medium, the particles experience less resistance, which results in more intensive interparticle contacts. Conversely, in the submerged case, the presence of a fluid significantly alters the dynamics. The fluid introduces additional forces acting on the particles, such as drag and buoyancy. The increased drag force from the fluid resistance necessitates higher shear forces to maintain particle motion. This dynamic is further amplified by the viscosity and density of the fluid medium, which enhances the intensity of shear interactions.

3. Angle of repose

The dynamic angle of repose, θ_m, is defined as the maximum angle crossed by the local plane of the free grain surface and the
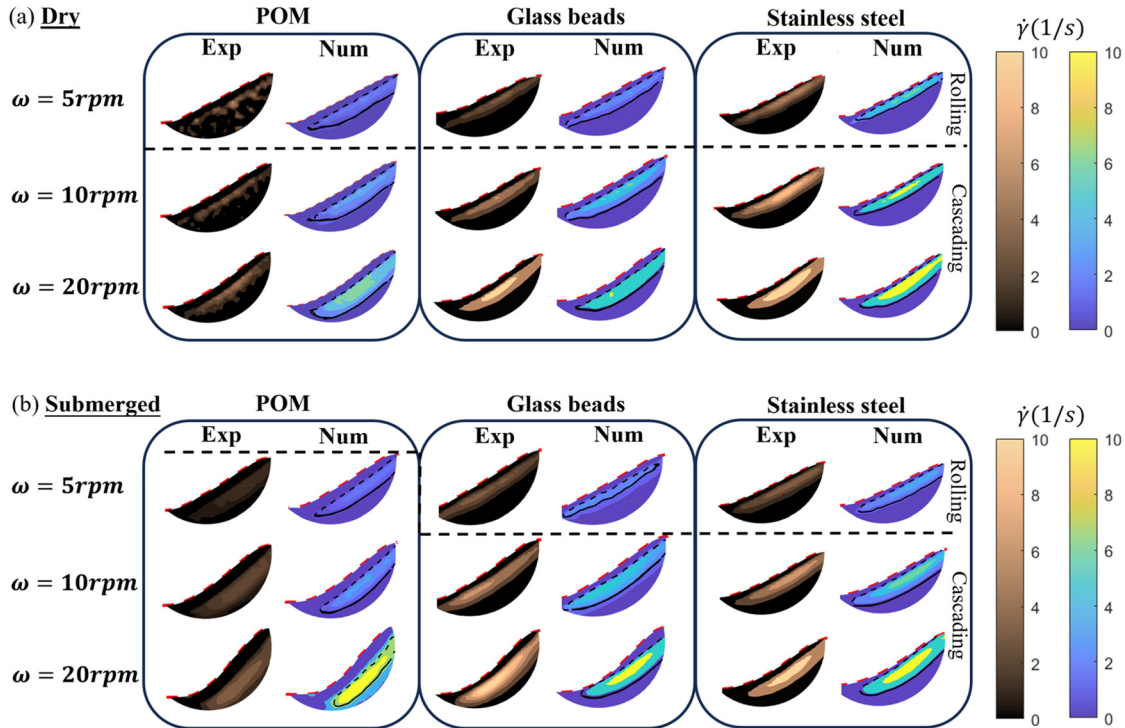
FIG. 3. Shear rate profile of the dry granular solid phase for POM particles, glass beads, and stainless steel particles from the left to the right and the comparison between experimental and numerical simulation results. The rolling and cascading regimes are differentiated by dashed lines. The red dashed line is the surface of the granular flow, and the black solid line represents the flow region interface. (a) dry granular flow and (b) submerged granular flow.

horizontal plane,[21,127] when the flow profile reaches an steady state wherein the whole grain surface grossly incline with a stable angle. Figures 4(a) and 4(b) show θ_m vs ω for various combinations of particles and ambient fluids. The fluid-particle mobility is a result of the competition between drag and gravity effects. The particulate drag force is determined by the drum rotation and ambient fluid. Specifically, the faster the drum rotates, the larger the drag becomes and, thus the steeper the free surface is, as also suggested in Refs. 21, 110, and 128, i.e., θ_m increases with ω. As for the ambient fluid, the drag force grows up significantly because of the higher fluid density and viscosity; therefore, an increase in θ_m in general can be observed by comparing Figs. 4(a) with 4(b). As a counterpart of drag force, effective gravity force is determined by the relative density, $\rho_s - \rho_f$. On the one hand, with increasing $\rho_s - \rho_f$, the gravity effect is amplified: the particle is falling downward more, resulting in the decrease in θ_m, as shown in Figs. 4(a) and 4(b). On the other hand, the effective stress also increases with higher $\rho_s - \rho_f$ and consequently the interparticle friction could be enlarged, inducing the increase in θ_m. In the low-ω regime, the effect of density difference will be dominant, since the drag force is too weak and counteract the gravity effect. Therefore, it is observed that at around $\omega = 5$–10 rpm, from air to water, θ_m of stainless-steel particles becomes slightly smaller because of the decrease in $\rho_s - \rho_f$.

To capture the combined effects of inertial and buoyancy forces, we introduce a modified Froude number with the consideration of density difference,

$$Fr^* = \sqrt{\frac{\rho_s \omega^2 R}{g(\rho_s - \rho_f)}}. \tag{15}$$

The subfigure inset in Fig. 5(a) indicates the relationship between $Fr^*(1 + 1/St)$ and θ_m/θ_{ave}. It demonstrates a trend that θ_m/θ_{ave} increases with $Fr^*(1 + 1/St)$ for both dry and submerged granular flows. In Ref. 16, θ_m for various grain sizes and properties and drum thicknesses was scaled with $Fr^*(1 + 1/St)$; herein, we confirm such a universality in dry flows. However, the scaling diminishes when fluid property comes into play. Building upon their finding, we normalized θ_m by θ_{ave}, which is determined by quasi-static rotating and influenced by grain inertia and fluid viscosity, to concentrate on effects of η_f, and employed Fr^* directly in the main plot of Fig. 5(a). Therein, a great collapse occurs to the data, where $\theta_m/\theta_{ave} \sim Fr^*$, regardless of particle and fluid properties. Meanwhile, for submerged stainless-steel flow at the maximum $Fr^* \approx 0.6$, θ_m/θ_{ave} slightly decreases; this is because at such higher Fr^* induced by fast rotating speed, ω, the cascading regime of interest has been transformed to cataracting regime, ruining the universality in the "tumbling" regimes of the median ω. Although according to Ref. 106, $Fr^* \in [0.06, 0.6]$ in this study encompasses the rolling and cascading flow regimes, the cataracting regime is clearly encountered at the highest Fr^*; individual grains are detached from the bed and thrown off into the free space of the drum.
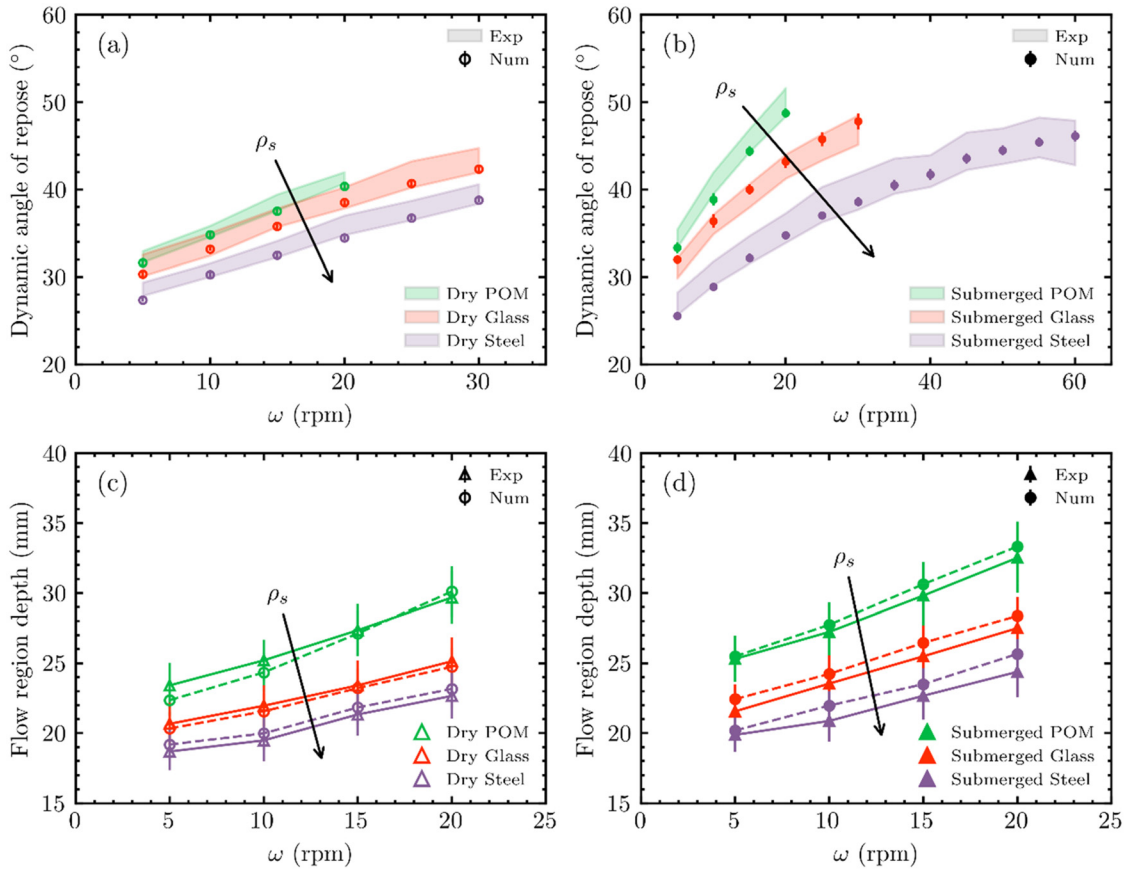
FIG. 4. Dynamic angle of repose θ_m (a) and (b) and flow region depth h (c) and (d) vs rotating speed ω across different granular materials under dry [(a) and (c)] and submerged [(b) and (d)] conditions. The shaded areas represent the average plus or minus one standard deviation of experimental results.
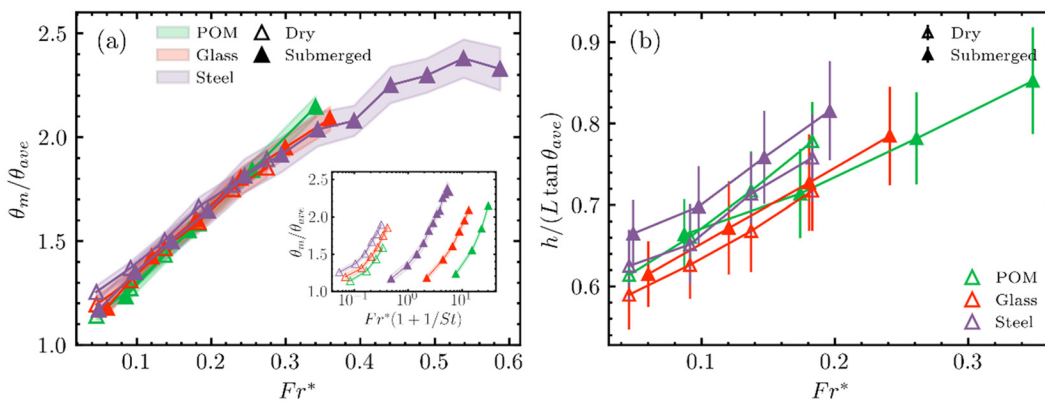

FIG. 5. Correlations between the flowing surface profile and the modified Froude number (Fr^*) based on the experimental data only: (a) is for normalized θ_m by θ_{ave}, where $\theta_{ave} = \tan^{-1}\left((\mu_s + \mu_d)/2\right)$, while (b) is for normalized h by $L \cdot \tan\theta_{stop}$, where L is the half length of the granular surface at the initial packing state before being rotated. The shaded areas represent the average plus or minus one standard deviation. $St = d^{1.5}\sqrt{\Delta\rho g\rho_s}/(18\eta_f)$ is the Stoke number[16,51] to denote the relative importance of grain inertia to fluid viscosity.

4. Flow region depth

Underneath the flowing layer surface, the flow within these drums can be categorized into two regions, namely, active and passive regions, as illustrated in Fig. 1(b). The "active region" is situated near the free surface, which flows freely downward due to gravitational forces. Conversely, deeper within the drum lies the "passive region" where particles move primarily, influenced by the rotating speed. Such two regions are separated by the grain layer with zero rotating and moving speeds. Specifically, "flow region depth" is defined as the maximum distance between the flowing layer surface and the interface, shown as red dashed and black solid lines in Fig. 3. The interface is sandwiched by the active and passive regions, thereby capturing the transition trend between these two regions.

The relationship between the flow region depth, h, and rotating speed is depicted in Figs. 4(c) and 4(d) for both dry and submerged granular flow. In both conditions, the increase in the rotating speed facilitates a more extensive distribution of dynamic forces across the drum, enhancing not only the shear rate but also expanding the area over which these interactions occur. Consequently, h is broadened. In contrast, higher particle densities could shorten h. This reduction occurs because the heavier packed particles have reduced lateral movement and increased vertical movement, due to increased particle inertia, which confines the interactions to a more concentrated area in the nominal drum area. The comparison between dry and submerged cases reveals that the submerged case exhibits a higher flow region depth. Also, the submerged granular flow in Fig. 4(d) demonstrates similar trends with the dry case shown in Fig. 4(c), but with notably steeper increases, especially evident for glass beads and POM spheres. The presence of a fluid medium introduces additional forces such as buoyancy and drag, enhancing the flow dynamics and leading to more pronounced changes in h with increased rotating speed.

In addition, Fig. 5(b) shows the gross linearity between Fr^* and the normalized active flow region depth, $h/(L\tan\theta_{ave})$.

Our findings in both Secs. III A 3 and III A 4 indicate the modified Froude number, Fr^*, is effective in capturing the complex combinations between inertia and buoyancy forces to quantify flow mobility in the rotating drum, regardless of fluid properties. The innovation of this study is that the submerged case exhibits heightened sensitivity due to additional forces, particularly pore pressure effects. Such an explanation necessities well documenting micro roots of fluid–solid interactions, which would be conducted in Sec. III B.

B. Numerical simulations

The focus of this section is on the numerical simulation, to supplement micro pore pressure distribution, which is hard to be measured in experimental manners. By comparing macro phenomenon including dynamic angle of repose and active flow region depth, validations are

TABLE III. Particle properties and input parameters in numerical simulations.

Material	Density (kg/m³)	μ_d	μ_s
Polyoxymethylene (POM)	1382	0.72	0.39
Glass beads	2363	0.64	0.38
Stainless steel	7803	0.54	0.33

conducted at first specificized for all the experiments in Sec. III A. With the micro information, we could gain deeper insight on why and how the modified Froude number could be well correlated with macro quantifications.

1. Validation

We first validate our numerical model against the experimental results concerning the shear rate distributions, angle of repose, and flow region depth, in Figs. 3 and 4. The details on the rheology model parameters can be found in Table III, where the particle property-related rheological parameters, including the solid phase filling rate, are measured directly from experiments. The comparison between experimental data and CFD predictions founded on the $\mu(I)$ rheology model illustrates the excellent quantitative agreement across all scenarios. In our experiments, the inner walls of the drum are treated with a rough coating to minimize slipping. Given the solid fraction in this study (~ 0.252), little slippage may occur;[63,80] therefore, the non-slip boundary condition is applied in our simulations.

2. Pressure distribution

Compared with experiments, the advantage within the Eulerian–Eulerian framework lies in accurately measuring the pore fluid and the solid pressure in submerged granular flows. Unlike air in the dry experiment, water in submerged granular flows has the unneglected density and the viscosity, resulting in negligible additional drag force on grains. Figure 6 shows both solid pressures, p_s, and pore fluid pressure, p_f, distributions at the steady stage. Both pressure increase rapidly with the higher particle density, while the rotating speed induces limited amplifications of them at median and high densities. This is attributed to the enhanced interaction forces and momentum exchange between the fluid phase and the granular phase of higher densities. We also observed concentrations of both fields of p_s and p_f at the bottom of the drum due to the cumulative effect of gravity. Another clear observation is that p_f is much higher than p_s, i.e., $p_f \approx 7p_s$, indicating the dominant effects of p_f in two-phase granular flows. This observation necessities a quantitatively statistical analysis of p_f for all simulated cases influenced by granular material density and rotating speed.

In Fig. 7, relations between the local solid fraction, ϕ_s, and the corresponding p_f for POM, glass, and stainless-steel spheres are plotted at various rotating speeds, ω. Like the finding in pressure distributions in Fig. 6, material density does dominate the local p_f. Meanwhile, for the same granular phase, the deviation induced by increasing ω diminishes; this is because, with the heavier drag force generated by higher ω and the constant gravitational force, larger p_f is needed for the force balance on the internal grains. However, local p_f cannot be enlarged unlimitedly, and its distribution tends to be stabilized; therefore, the flow pattern transition occurs from the flat (at rolling regimes) to the "S" (at cascading regimes) shapes for the new balance state. Finally, a final converged distribution of p_f could be encountered, which is also demonstrated by p_f within the steel granular phase in Fig. 6.

IV. DISCUSSIONS
A. Pore fluid pressure scaling

As mentioned above, the fluid pressure, p_f, influenced by the external factors including rotating speed and particle density, has more superior effects than solid pressure in the granular flow. Meanwhile,
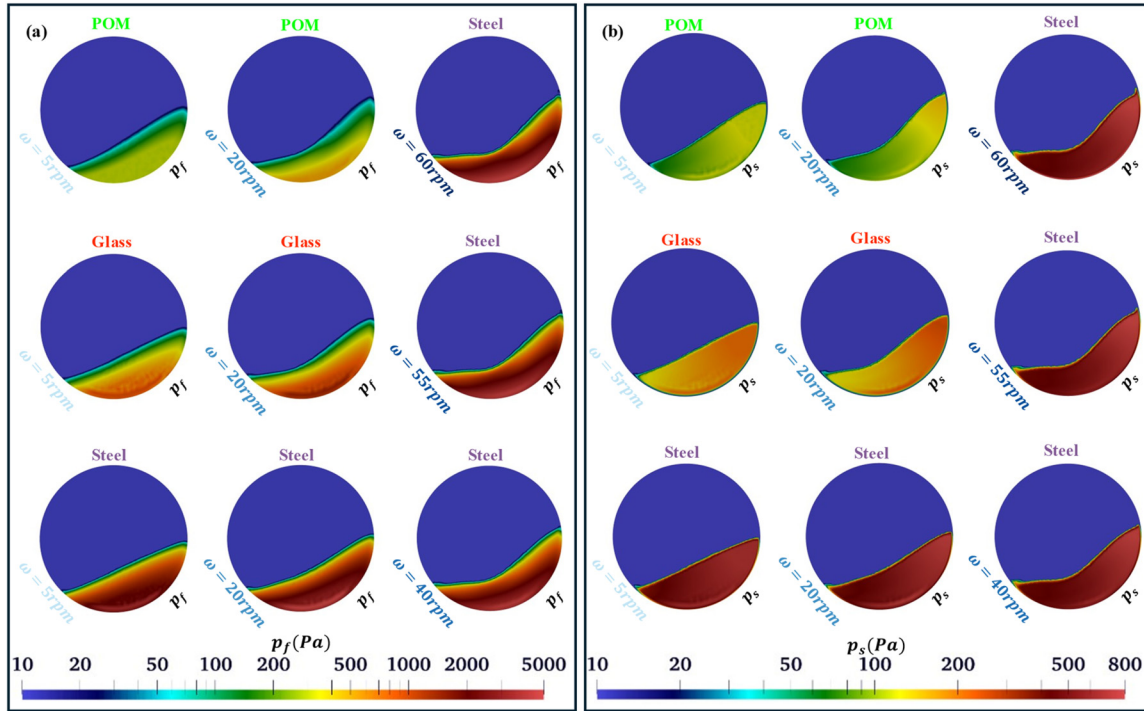
FIG. 6. Pressure distributions as predicted by the proposed model under submerged conditions for different materials at varying rotating speeds: (a) pore fluid pressure and (b) solid pressure.

the intrinsic properties, such as the fluid viscosity and fluid density, of the fluid itself also play a significant role in distributions of p_f. To unify all these effects, we nondimensionalize p_f by involving in the drag force, associated with rotating speed and the viscous effect, and the effective inertial force $\sqrt{\rho_f(\rho_s - \rho_f)gd}$ on both the fluid phase and solid phase,

FIG. 7. Comparisons of mean local fluid pressure at the specific granular volume fraction within the mixed phases for different materials and rotating speeds. The data points represent the average fluid pressure calculated at volume fraction intervals of 0.01, with standard deviations depicted as error bars.

$$K = \frac{p_f}{Re^{1/2}\sqrt{\rho_f(\rho_s - \rho_f)gd}}, \quad (16)$$

where K is the dimensionless pore pressure number and $Re = \rho_f \omega R d_s/\mu_f$ is the Reynolds number. Compared with the particle Reynolds number, $Re_s = \rho_f|U_f - U_s|d_s/\mu_f$, where ωR is utilized instead of $|U_f - U_s|$ to consider the global flow behavior of grains in the whole drum.

As illustrated in Fig. 8, K is well correlated with the local solid fraction, ϕ_s, or local porosity, $\phi_f = 1 - \phi_s$. Interestingly, if linear regression is conducted, the slope indicates that $K \propto \phi_s{}^2/\phi_f{}^3$, of which the right item is also in the Kozeny–Carman (KC) equation[129] to predict permeability through nonoverlapped-sphere porous media. Such a linearity implies that as the porosity decreases, K is exponentially reduced due to the increased flow resistance encountered by more relative movements between the fluid and the tighter particle arrangements.

This concordance suggests that K can be interpreted as a function of ϕ_s in the fashion like predicting permeability coefficient, although within the rotating drum, the rotational dynamics and fluid–solid interactions are unique to those of densely packed, static grains in the KC equation. As it captures the combined effects of inertia and the system's rotational energy, similar scaling also holds for the dry granular flow. It indicates that the KC equation might remain valid in predicting drag coefficient when the grain movement comes into play. It extends the applicability of the KC relationship, emphasizing its utility in the analysis of complex-phased granular systems beyond the conventionally static bed configurations. However, the proposed
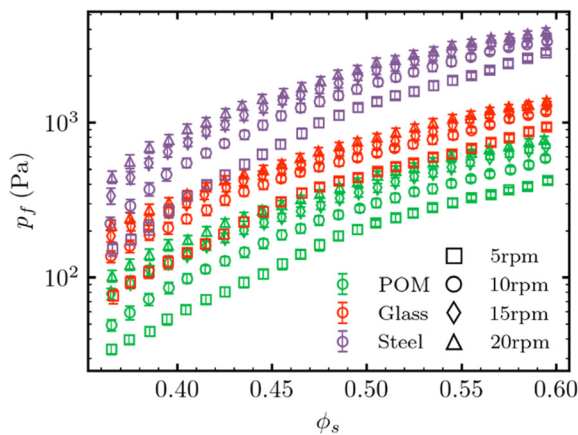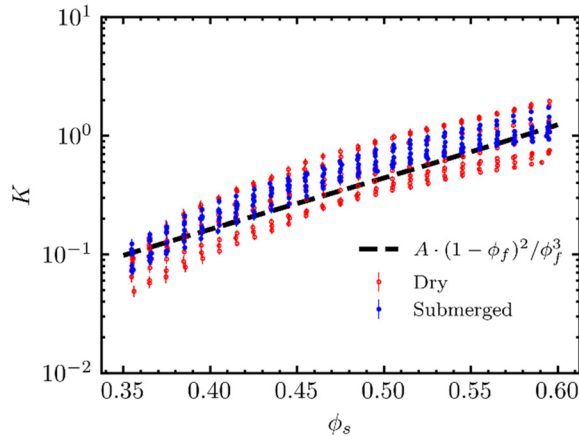
FIG. 8. The correlation between normalized local pore pressure and volume fraction of solid phase. The black dash line depicts the theoretical fit based on the Kozeny–Carman equation.

FIG. 9. Normalized solid fraction vs G for submerged and dry cases with $\omega = 10$ rpm. The dashed line represents the theoretical relationship between rheological parameters as proposed by Ge *et al.*[76]

correlation is limited to the simulation conditions used in this study. The mono-sized systems used in this study represent the minimal case for the general granular flow, highlighting the contributions from the controllable factors, such as the relative density, pore fluids, and rotating speeds. In practice, however, polydisperse systems are often encountered in granular flow warranting future studies with a specific focus on the contributions from the grain size distributions. Further studies are needed to incorporate more parameters, such as the particle size and shape.

B. Scaling with $\mu(G)$ rheology

In our study, we have extended the validation of our numerical model to demonstrate its alignment not only with the $\mu(I)$ rheology but also with the $\mu(G)$ rheology, as suggested by Ge *et al.*[76] Compared with the inertial number, $I = \dot{\gamma} d_s / \sqrt{p_s / \rho_s}$, as a single dimensionless ratio of micro inertial, $\sqrt{\rho_s d_s^2 / p_s}$, to macro, $1/\dot{\gamma}$, time scales, Cassar *et al.*[47] extended this to submerged flow by using a viscous timescale, η_f / p_s, instead of $\sqrt{\rho_s d_s^2 / p_s}$, the resulting ratio is $J = \dot{\gamma} \eta_f / p_s$. The combined influences of I and J could be used to predict the global solid fraction for both dry and wet granular flows:[76] $\phi_s = \phi_c(1 - bG^{0.5})$, where ϕ_c is the fitted critical solid fraction, b the fitting parameter, $G(p_s, \dot{\gamma}, \rho_s, \eta_f, d_s) = 12(J + \lambda(St') \cdot I^2)$, and $\lambda(St') = (1 - e^{-18/St'})/(18 - St' \cdot (1 - e^{-18/St'}))$. Here, we check whether, for the first time, such a global scaling law could be fixed to local granular rheology at every mesh point in our continuum simulations, as shown in Fig. 9. For the illustrative purpose and without loss generality, three types of submerged and one type of dry flows with the same $\omega = 10$ rpm are involved in Fig. 8. A power law does exist between $1 - \phi_s/\phi_c$ and G, but the exponents are all about 0.1 far less than 0.5. Although the rigidity of such a continuum finding deserves extensive validations, i.e., using combined CFD-DEM framework to better capture grain-scale solid–liquid interactions, at least the reliability of our two-phase model across different ambient fluid conditions and grains is validated.
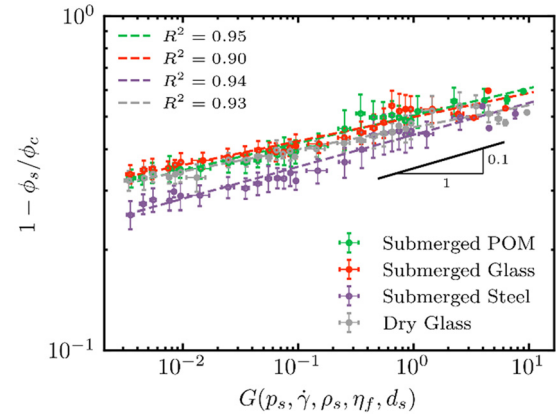
V. CONCLUSIONS

In this work, we investigate granular flows in rotating drums using both numerical and experimental approaches. Different rotating speeds, particle densities, and fluid properties are applied. The granular flow is modeled as a continuum represented by the $\mu(I)$ theory, with parameters derived from extensive experimental datasets. Following this study, the following main conclusions are summarized:

- The numerical simulations, combining with $\mu(I)$ rheology theory, are validated by substantial experiment results and thus could successfully capture the succession of granular flow regimes both macroscopically and microscopically.
- We propose a modified Froude number that effectively captures the combination effect of grain inertia and buoyancy forces irrespective of fluid viscosities, to linearly relate the dynamic angle of repose at the rolling and the cascading regimes. It enhances our understanding to differentiate between flow patterns under varying conditions.
- Compared with dry flow in rotating drums, the pore pressure that is much higher than the solid pressure in the wet flow dominates the flow mobility. It is primarily determined by grain densities and enlarged by rotating speeds; however, the pore pressure distribution could saturate with high rotating speeds, at which the flow regime/pattern transits from the cascading to cataracting mode.
- A dimensionless number characterizing the local pore pressure is proposed to quantify its dependence on porosity. Such a number is grossly linear to the porosity function in the Kozeny–Carman equation for predicting permeability coefficients of granular porous media.
- The generality of combining $\mu(I)$ and $\mu(G)$ theories into one number, i.e., $G(p_s, \dot{\gamma}, \rho_s, \eta_f, d_s) = 12(J + \lambda(St') \cdot I^2)$, to link global variables, i.e., $\phi_s = \phi_c(1 - bG^{0.5})$, is locally examined. A power law does exist between $1 - \frac{\phi_s}{\phi_c}$ and G, but the constant exponent in both dry and wet rotating drums is ≈ 0.1 and much lower than 0.5.

In this study, the particles are in a relatively large size with a narrow diameter distribution to simplify the analysis and highlight the core rheological behaviors, and the cohesionless granular flow neglects the

electrostatic and van der Walls forces. However, many industrial applications often involve particles with a wider range of sizes and may contain smaller sizes, where these cohesive forces may dominate. While our results provide insights into the fundamental dynamics of granular flow, further improvements under the two-phase flow framework should extend to a broader size distribution and incorporate cohesive forces, to provide a more comprehensive understanding of flow behaviors such as mixing, segregation, agglomeration, and other dynamic responses.

ACKNOWLEDGMENTS

AUTHOR DECLARATIONS
Conflict of Interest

The authors have no conflicts to disclose.

Author Contributions

Yu Chen: Conceptualization (equal); Formal analysis (equal); Methodology (lead); Visualization (equal); Writing – original draft (lead). **Si Suo:** Formal analysis (equal); Supervision (equal); Visualization (supporting); Writing – review & editing (equal). **Mingrui Dong:** Formal analysis (supporting); Writing – review & editing (supporting). **Haiyi Zhong:** Writing – review & editing (supporting). **Deheng Wei:** Conceptualization (equal); Formal analysis (equal); Visualization (lead); Writing – original draft (equal). **Yixiang Gan:** Conceptualization (lead); Formal analysis (equal); Methodology (equal); Supervision (lead); Writing – review & editing (equal).

DATA AVAILABILITY

The data that support the findings of this study are available from the corresponding authors upon reasonable request.

REFERENCES

[1]J. Schweizer, J. Bruce Jamieson, and M. Schneebeli, "Snow avalanche formation," Rev. Geophys. **41**, 1016, https://doi.org/10.1029/2002RG000123 (2003).

[2]P. Bartelt and B. W. McArdell, "Granulometric investigations of snow avalanches," J. Glaciol. **55**, 829–833 (2009).

[3]D. Jessop, K. Kelfoun, P. Labazuy, A. Mangeney, O. Roche, J.-L. Tillier, M. Trouillet, and G. Thibault, "LiDAR derived morphology of the 1993 Lascar pyroclastic flow deposits, and implication for flow dynamics and rheology," J. Volcanol. Geotherm. Res. **245**, 81–97 (2012).

[4]A. Lucas, A. Mangeney, and J. P. Ampuero, "Frictional velocity-weakening in landslides on Earth and on other planetary bodies," Nat. Commun. **5**, 3417 (2014).

[5]T. Takahashi, "Mechanical characteristics of debris flow," J. Hydraul. Div. **104**, 1153–1169 (1978).

[6]K. Hutter, B. Svendsen, and D. Rickenmann, "Debris flow modeling: A review," Continuum Mech. Thermodyn. **8**, 1–35 (1994).

[7]M. Hürlimann, V. Coviello, C. Bel, X. Guo, M. Berti, C. Graf, J. Hübl, S. Miyata, J. B. Smith, and H.-Y. Yin, "Debris-flow monitoring and warning: Review and examples," Earth-Sci. Rev. **199**, 102981 (2019).

[8]J. M. Ottino and D. V. Khakhar, "Fundamental research in heaping, mixing, and segregation of granular materials: Challenges and perspectives," Powder Technol. **121**, 117–122 (2001).

[9]P. Porion, N. Sommier, A.-M. Faugère, and P. Evesque, "Dynamics of size segregation and mixing of granular materials in a 3D-blender by NMR imaging investigation," Powder Technol. **141**, 55–68 (2004).

[10]S. L. Conway, A. Lekhal, J. G. Khinast, and B. J. Glasser, "Granular flow and segregation in a four-bladed mixer," Chem. Eng. Sci. **60**, 7091–7107 (2005).

[11]J. M. N. T. Gray and C. Ancey, "Particle-size and -density segregation in granular free-surface flows," J. Fluid Mech. **779**, 622–668 (2015).

[12]T. Yao, H. Yang, S. D. N. Lourenço, B. A. Baudet, and F. C. Y. Kwok, "Multi-scale particle morphology evolution in rotating drum tests: Role of particle shape and pore fluid," Eng. Geol. **303**, 106669 (2022).

[13]M. Yamamoto, S. Ishihara, and J. Kano, "Evaluation of particle density effect for mixing behavior in a rotating drum mixer by DEM simulation," Adv. Powder Technol. **27**, 864–870 (2016).

[14]H. T. Chou, S. H. Chou, and S. S. Hsiau, "The effects of particle density and interstitial fluid viscosity on the dynamic properties of granular slurries in a rotating drum," Powder Technol. **252**, 42–50 (2014).

[15]S. B. Savage, M. H. Babaei, and T. Dabros, "Modeling gravitational collapse of rectangular granular piles in air and water," Mech. Res. Commun. **56**, 1–10 (2014).

[16]F. Pignatel, C. Asselin, L. Krieger, I. C. Christov, J. M. Ottino, and R. M. Lueptow, "Parameters and scalings for dry and immersed granular flowing layers in rotating tumblers," Phys. Rev. E **86**, 011304 (2012).

[17]O. Pouliquen, "Scaling laws in granular flows down rough inclined planes," Phys. Fluids **11**, 542–548 (1999).

[18]C. Ancey, "Dry granular flows down an inclined channel: Experimental investigations on the frictional-collisional regime," Phys. Rev. E **65**, 011304 (2001).

[19]Y.-J. Jiang, X.-Y. Fan, T.-H. Li, and S.-Y. Xiao, "Influence of particle-size segregation on the impact of dry granular flow," Powder Technol. **340**, 39–51 (2018).

[20]U. D'Ortona and N. Thomas, "Self-induced Rayleigh-Taylor instability in segregating dry granular flows," Phys. Rev. Lett. **124**, 178001 (2020).

[21]M. Dong, Z. Wang, B. Marks, Y. Chen, and Y. Gan, "Partially saturated granular flow in a rotating drum: The role of cohesion," Phys. Fluids **35**, 113302 (2023).

[22]C. Yuan, M. Moscariello, S. Cuomo, and B. Chareyre, "Numerical simulation of wetting-induced collapse in partially saturated granular soils," Granular Matter **21**, 64 (2019).

[23]P. Si, H. Shi, and X. Yu, "Development of a mathematical model for submarine granular flows," Phys. Fluids **30**, 083302 (2018).

[24]C. M. Dury and G. H. Ristow, "Competition of mixing and segregation in rotating cylinders," Phys. Fluids **11**, 1387–1394 (1999).

[25]E. Alizadeh, O. Dubé, F. Bertrand, and J. Chaouki, "Characterization of mixing and size segregation in a rotating drum by a particle tracking method," AIChE J. **59**, 1894–1905 (2013).

[26]G. Seiden and P. J. Thomas, "Complexity, segregation, and pattern formation in rotating-drum flows," Rev. Mod. Phys. **83**, 1323–1365 (2011).

[27]F. Melo and S. Douady, "From solitary waves to static patterns via spatiotemporal intermittency," Phys. Rev. Lett. **71**, 3283 (1993).

[28]O. A. M. Boote and P. J. Thomas, "Effects of granular additives on transition boundaries between flow states of rimming flows," Phys. Fluids **11**, 2020–2029 (1999).

[29]H. Jaeger, C.-H. Liu, and S. R. Nagel, "Relaxation at the angle of repose," Phys. Rev. Lett. **62**, 40 (1989).

[30]J. M. Ottino and D. V. Khakhar, "Mixing and segregation of granular materials," Annu. Rev. Fluid Mech. **32**, 55–91 (2000).

[31]A. W. Nienow, M. F. Edwards, and N. Harnby, *Mixing in the Process Industries* (Butterworth-Heinemann, 1997).

[32]N. Sommier, P. Porion, P. Evesque, B. Leclerc, P. Tchoreloff, and G. Couarraze, "Magnetic resonance imaging investigation of the mixing-segregation process in a pharmaceutical blender," Int. J. Pharm. **222**, 243–258 (2001).

[33]S. Massol-Chaudeur, H. Berthiaux, and J. A. Dodds, "Experimental study of the mixing kinetics of binary pharmaceutical powder mixtures in a laboratory hoop mixer," Chem. Eng. Sci. **57**, 4053–4065 (2002).

[34]S. Badar and I. H. Farooqi, "Pulp and paper industry—Manufacturing process, wastewater generation and treatment," in *Environmental Protection Strategies for Sustainable Development* (Springer, 2012), pp. 397–436.

[35]C. S. Campbell, "Granular material flows—An overview," Powder Technol. **162**, 208–229 (2006).

[36]M. J. Vold, "The effect of adsorption on the van der Waals interaction of spherical colloidal particles," J. Colloid Sci. **16**, 1–12 (1961).

[37]J. Q. Feng and D. A. Hays, "Relative importance of electrostatic forces on powder particles," Powder Technol. **135**, 65–75 (2003).

[38]Q. T. Phan, H. H. Bui, and G. D. Nguyen, "Modeling submerged granular flow across multiple regimes using the Eulerian–Eulerian approach with shear-induced volumetric behavior," Phys. Fluids **34**, 063308 (2022).

[39]A. Tripathi and D. V. Khakhar, "Density difference-driven segregation in a dense granular flow," J. Fluid Mech. **717**, 643–669 (2013).

[40]Z. Miao, T. E. Grift, A. C. Hansen, and K. C. Ting, "Flow performance of ground biomass in a commercial auger," Powder Technol. **267**, 354–361 (2014).

[41]C. Meruane, A. Tamburrino, and O. Roche, "On the role of the ambient fluid on gravitational granular flow dynamics," J. Fluid Mech. **648**, 381–404 (2010).

[42]C.-H. Lee and Z. Huang, "A two-phase flow model for submarine granular flows: With an application to collapse of deeply-submerged granular columns," Adv. Water Resour. **115**, 286–300 (2018).

[43]G. Juarez, P. Chen, and R. M. Lueptow, "Transition to centrifuging granular flow in rotating tumblers: A modified Froude number," New J. Phys. **13**, 053055 (2011).

[44]G. G. D. Zhou, K. F. E. Cui, L. Jing, T. Zhao, D. Song, and Y. Huang, "Particle size segregation in granular mass flows with different ambient fluids," J. Geophys. Res. **125**, e2020JB019536, https://doi.org/10.1029/2020JB019536 (2020).

[45]H. Kalman and D. Portnikov, "Analyzing bulk density and void fraction: A. The effect of archimedes number," Powder Technol. **381**, 477–487 (2021).

[46]N. Jain, D. V. Khakhar, R. M. Lueptow, and J. M. Ottino, "Self-organization in granular slurries," Phys. Rev. Lett. **86**, 3771 (2001).

[47]C. Cassar, M. Nicolas, and O. Pouliquen, "Submarine granular flows down inclined planes," Phys. Fluids **17**, 103301 (2005).

[48]C. C. Liao, S. S. Hsiau, and H. C. Nien, "Effects of density ratio, rotation speed, and fill level on density-induced granular streak segregation in a rotating drum," Powder Technol. **284**, 514–520 (2015).

[49]T. Barker, M. Rauter, E. S. F. Maguire, C. G. Johnson, and J. M. N. T. Gray, "Coupling rheology and segregation in granular flows," J. Fluid Mech. **909**, A22 (2020).

[50]R. A. Bagnold, "The flow of cohesionless grains in fluids," Philos. Trans. R. Soc., A **249**, 235–297 (1956).

[51]S. Courrech du Pont, P. Gondret, B. Perrin, and M. Rabaud, "Granular avalanches in fluids," Phys. Rev. Lett. **90**, 044301 (2003).

[52]J. A. Garcia Aragon, "Granular-fluid chute flow: Experimental and numerical observations," J. Hydraul. Eng. **121**, 355–364 (1995).

[53]A. Armanini, H. Capart, L. Fraccarollo, and M. Larcher, "Rheological stratification in experimental free-surface flows of granular–liquid mixtures," J. Fluid Mech. **532**, 269–319 (2005).

[54]E. L. Thompson and H. E. Huppert, "Granular column collapses: Further experimental results," J. Fluid Mech. **575**, 177–186 (2007).

[55]C.-H. Lee, Z. Huang, and M.-L. Yu, "Collapse of submerged granular columns in loose packing: Experiment and two-phase flow simulation," Phys. Fluids **30**, 123307 (2018).

[56]M. Cabrera and N. Estrada, "Granular column collapse: Analysis of grain-size effects," Phys. Rev. E **99**, 012905 (2019).

[57]F. Ceccato, A. Leonardi, V. Girardi, P. Simonini, and M. Pirulli, "Numerical and experimental investigation of saturated granular column collapse in air," Soils Found. **60**, 683–696 (2020).

[58]S. H. Chou, C. C. Liao, and S. S. Hsiau, "An experimental study on the effect of liquid content and viscosity on particle segregation in a rotating drum," Powder Technol. **201**, 266–272 (2010).

[59]T. El Geitani and B. Blais, "Solid-liquid rotary kilns: An experimental and CFD-DEM study," Powder Technol. **430**, 119008 (2023).

[60]M. Jiang, Y. Zhao, G. Liu, and J. Zheng, "Enhancing mixing of particles by baffles in a rotating drum mixer," Particuology **9**, 270–278 (2011).

[61]F. Yu, G. Zhou, J. Xu, and W. Ge, "Enhanced axial mixing of rotating drums with alternately arranged baffles," Powder Technol. **286**, 276–287 (2015).

[62]B. Liu, Q. Wang, Z. Zhou, and R. Zou, "Influence of baffles on mixing and heat transfer characteristics in an internally heated rotating drum," Powder Technol. **398**, 117129 (2022).

[63]D. A. Santos, I. J. Petri, C. R. Duarte, and M. A. S. Barrozo, "Experimental and CFD study of the hydrodynamic behavior in a rotating drum," Powder Technol. **250**, 52–62 (2013).

[64]R. J. Brandao, R. M. Lima, R. L. Santos, C. R. Duarte, and M. A. A. Barrozo, "Experimental study and DEM analysis of granular segregation in a rotating drum," Powder Technol. **364**, 1–12 (2020).

[65]X. Xiao, Y. Tan, H. Zhang, R. Deng, and S. Jiang, "Experimental and DEM studies on the particle mixing performance in rotating drums: Effect of area ratio," Powder Technol. **314**, 182–194 (2017).

[66]X. Liu, W. Ge, Y. Xiao, and J. Li, "Granular flow in a rotating drum with gaps in the side wall," Powder Technol. **182**, 241–249 (2008).

[67]X. Liu, W. Ma, Q. Hou, Q. Zhang, B. Gong, and Y. Feng, "End-wall effects on the mixing process of granular assemblies in a short rotating drum," Powder Technol. **339**, 497–505 (2018).

[68]A. Jain, F. Evrard, and B. van Wachem, "The effect of side walls on particles mixing in rotating drums," Particuology **72**, 112–121 (2023).

[69]C.-H. Lee, "Two-phase modelling of submarine granular flows with shear-induced volume change and pore-pressure feedback," J. Fluid Mech. **907**, A31 (2020).

[70]L. Amoudry, T. J. Hsu, and P. L.-F. Liu, "Two-phase model for sand transport in sheet flow regime," J. Geophys. Res. **113**, C03011, https://doi.org/10.1029/2007JC004179 (2008).

[71]A.-N. Huang and H.-P. Kuo, "CFD simulation of particle segregation in a rotating drum. Part I: Eulerian solid phase kinetic viscosity," Adv. Powder Technol. **28**, 2094–2101 (2017).

[72]W. Rong, Y. Feng, P. Schwarz, P. Witt, B. Li, T. Song, and J. Zhou, "Numerical study of the solid flow behavior in a rotating drum based on a multiphase CFD model accounting for solid frictional viscosity and wall friction," Powder Technol. **361**, 87–98 (2020).

[73]Q. J. Zheng and A. B. Yu, "Modelling the granular flow in a rotating drum by the Eulerian finite element method," Powder Technol. **286**, 361–370 (2015).

[74]Q. Zheng, Y. Tian, W. Wang, J. Ye, Q. Zheng, and S. Kuang, "CFD simulation of a cement precalciner with agglomerate-based drag modeling," Powder Technol. **436**, 119508 (2024).

[75]P. Jop, Y. Forterre, and O. Pouliquen, "A constitutive law for dense granular flows," Nature **441**, 727–730 (2006).

[76]Z. Ge, T. Man, H. E. Huppert, K. M. Hill, and S. A. Galindo-Torres, "Unifying length-scale-based rheology of dense suspensions," Phys. Rev. Fluids **9**, L012302 (2024).

[77]M. Trulsson, B. Andreotti, and P. Claudin, "Transition from the viscous to inertial regime in dense suspensions," Phys. Rev. Lett. **109**, 118305 (2012).

[78]F. Tapia, M. Ichihara, O. Pouliquen, and É. Guazzelli, "Viscous to inertial transition in dense granular suspension," Phys. Rev. Lett. **129**, 078001 (2022).

[79]J. S. Fannon, I. R. Moyles, and A. C. Fowler, "Application of the compressible I-dependent rheology to chute and shear flow instabilities," J. Fluid Mech. **864**, 1026–1057 (2019).

[80]A. M. G. Arseni, G. De Monaco, F. Greco, and P. L. Maffettone, "Granular flow in rotating drums through simulations adopting a continuum constitutive equation," Phys. Fluids **32**, 093305 (2020).

[81]B. Vowinckel, J. Withers, P. Luzzatto-Fegiz, and E. Meiburg, "Settling of cohesive sediment: Particle-resolved simulations," J. Fluid Mech. **858**, 5–44 (2019).

[82]K. Zhao, B. Vowinckel, T.-J. Hsu, T. Köllner, B. Bai, and E. Meiburg, "An efficient cellular flow model for cohesive particle flocculation in turbulence," J. Fluid Mech. **889**, R3 (2020).

[83]K. F. E. Cui, G. G. D. Zhou, L. Jing, X. Chen, and D. Song, "Generalized friction and dilatancy laws for immersed granular flows consisting of large and small particles," Phys. Fluids **32**, 113312 (2020).

[84]X. Tang, Y. Yue, S. Wang, and Y. Shen, "Modelling of gas-solid-liquid flow and particle mixing in a rotary drum," Powder Technol. **409**, 117758 (2022).

[85]L. Jing, G. C. Yang, C. Y. Kwok, and Y. D. Sobral, "Flow regimes and dynamic similarity of immersed granular collapse: A CFD-DEM investigation," Powder Technol. **345**, 532–543 (2019).

[86]J. Zhao and T. Shan, "Coupled CFD–DEM simulation of fluid–particle interaction in geomechanics," Powder Technol. **239**, 248–258 (2013).

[87]N. I. Ismail, S. Kuang, and A. Yu, "CFD-DEM study of particle-fluid flow and retention performance of sand screen," Powder Technol. **378**, 410–420 (2021).

[88]Y.-H. Sun, W.-T. Zhang, X.-L. Wang, and Q.-Q. Liu, "Numerical study on immersed granular collapse in viscous regime by particle-scale simulation," Phys. Fluids **32**, 073313 (2020).

[89]C. Peng, L. Zhan, W. Wu, and B. Zhang, "A fully resolved SPH-DEM method for heterogeneous suspensions with arbitrary particle shape," Powder Technol. **387**, 509–526 (2021).

[90]W.-J. Xu, X.-Y. Dong, and W.-T. Ding, "Analysis of fluid-particle interaction in granular materials using coupled SPH-DEM method," Powder Technol. **353**, 459–472 (2019).

[91]W.-J. Xu, Z.-G. Yao, Y.-T. Luo, and X.-Y. Dong, "Study on landslide-induced wave disasters using a 3D coupled SPH-DEM method," Bull. Eng. Geol. Environ. **79**, 467–483 (2020).

[92]K. Washino, E. L. Chan, T. Tsujimoto, T. Tsuji, and T. Tanaka, "Development of resolved CFD–DEM coupling model for three-phase flows with non-spherical particles," Chem. Eng. Sci. **267**, 118335 (2023).

[93]Z. Shen, G. Wang, D. Huang, and F. Jin, "A resolved CFD-DEM coupling model for modeling two-phase fluids interaction with irregularly shaped particles," J. Comput. Phys. **448**, 110695 (2022).

[94]Y. Tsuji, T. Kawaguchi, and T. Tanaka, "Discrete particle simulation of two-dimensional fluidized bed," Powder Technol. **77**, 79–87 (1993).

[95]Z. Y. Zhou, S. B. Kuang, K. W. Chu, and A. B. Yu, "Discrete particle simulation of particle–fluid flow: Model formulations and their applicability," J. Fluid Mech. **661**, 482–510 (2010).

[96]P. Kieckhefen, S. Pietsch, M. Dosta, and S. Heinrich, "Possibilities and limits of computational fluid dynamics–discrete element method simulations in process engineering: A review of recent advancements and future trends," Annu. Rev. Chem. Biomol. Eng. **11**, 397–422 (2020).

[97]E. P. Montellà, J. Chauchat, B. Chareyre, C. Bonamy, and T. J. Hsu, "A two-fluid model for immersed granular avalanches with dilatancy effects," J. Fluid Mech. **925**, A13 (2021).

[98]D. Schneider, R. Kaitna, W. E. Dietrich, L. Hsu, C. Huggel, and B. W. McArdell, "Frictional behavior of granular gravel–ice mixtures in vertically rotating drum experiments and implications for rock–ice avalanches," Cold Reg. Sci. Technol. **69**, 70–90 (2011).

[99]G. D. R. MiDi, "On dense granular flows," Eur. Phys. J. E. **14**, 341–365 (2004).

[100]J. Rajchenbach, "Flow in powders: From discrete avalanches to continuous regime," Phys. Rev. Lett. **65**, 2221 (1990).

[101]C. M. Dury, G. H. Ristow, J. L. Moss, and M. Nakagawa, "Boundary effects on the angle of repose in rotating cylinders," Phys. Rev. E **57**, 4491 (1998).

[102]K. Yamane, M. Nakagawa, S. A. Altobelli, T. Tanaka, and Y. Tsuji, "Steady particulate flows in a horizontal rotating cylinder," Phys. Fluids **10**, 1419–1427 (1998).

[103]G. H. Ristow, "Particle mass segregation in a two-dimensional rotating drum," Europhys. Lett. **28**, 97 (1994).

[104]S. H. Chou and S. S. Hsiau, "Dynamic properties of immersed granular matter in different flow regimes in a rotating drum," Powder Technol. **226**, 99–106 (2012).

[105]H. Henein, J. K. Brimacombe, and A. P. Watkinson, "Experimental study of transverse bed motion in rotary kilns," Metall. Trans. B **14**, 191–205 (1983).

[106]J. Mellmann, "The transverse motion of solids in rotating cylinders—forms of motion and transition behavior," Powder Technol. **118**, 251–270 (2001).

[107]C. S. Campbell, "Rapid granular flows," Annu. Rev. Fluid Mech. **22**, 57–90 (1990).

[108]Q. Zheng, Q. Luo, and A. Yu, "A unified theory for granular matter," Powder Technol. **434**, 119370 (2024).

[109]G. Félix, V. Falk, and U. D'Ortona, "Granular flows in a rotating drum: The scaling law between velocity and thickness of the flow," Eur. Phys. J. E **22**, 25–31 (2007).

[110]R. Y. Yang, A. B. Yu, L. McElroy, and J. Bao, "Numerical simulation of particle dynamics in different flow regimes in a rotating drum," Powder Technol. **188**, 170–177 (2008).

[111]O. Zik, D. Levine, S. G. Lipson, S. Shtrikman, and J. Stavans, "Rotationally induced segregation of granular materials," Phys. Rev. Lett. **73**, 644 (1994).

[112]D. V. Khakhar, J. J. McCarthy, and J. M. Ottino, "Radial segregation of granular mixtures in rotating cylinders," Phys. Fluids **9**, 3600–3614 (1997).

[113]R. Brewster, G. S. Grest, and A. J. Levine, "Effects of cohesion on the surface angle and velocity profiles of granular material in a rotating drum," Phys. Rev. E **79**, 011305 (2009).

[114]O. Roche, S. van den Wildenberg, A. Valance, R. Delannay, A. Mangeney, L. Corna, and T. Latchimy, "Experimental assessment of the effective friction at the base of granular chute flows on a smooth incline," Phys. Rev. E **103**, 042905 (2021).

[115]J. Du, G. G. Zhou, and K. F. Cui, "Microscopic description of basal stress generated by granular free-surface flows," J. Geophys. Res. **128**, e2022JF006953, https://doi.org/10.1029/2022JF006953 (2023).

[116]A. V. Orpe and D. Khakhar, "Scaling relations for granular flow in quasi-two-dimensional rotating cylinders," Phys. Rev. E **64**, 031302 (2001).

[117]H. R. Norouzi, R. Zarghami, and N. Mostoufi, "Insights into the granular flow in rotating drums," Chem. Eng. Res. Des. **102**, 12–25 (2015).

[118]H.-T. Chou and C.-F. Lee, "Cross-sectional and axial flow characteristics of dry granular material in rotating drums," Granular Matter **11**, 13–32 (2008).

[119]W. Thielicke and R. Sonntag, "Particle Image Velocimetry for MATLAB: Accuracy and enhanced algorithms in PIVlab," J. Open Res. Software **9**, 12 (2021).

[120]H. Jasak, A. Jemcov, and Z. Tukovic, "OpenFOAM: A C++ library for complex physics simulations," International workshop on coupled methods in numerical dynamics, 2007.

[121]P. G. Saffman, "The lift on a small sphere in a slow shear flow," J. Fluid Mech. **22**, 385–400 (1965).

[122]T. R. Auton, *Dynamics of bubbles, Drops, and Particles in Motion in Liquids*, Fluid Mechanics and Its Applications (Springer, 1984).

[123]D. Gidaspow, *Multiphase Flow and Fluidization: Continuum and Kinetic Theory Descriptions* (Academic Press, 1994).

[124]Y. Forterre and O. Pouliquen, "Flows of dense granular media," Annu. Rev. Fluid Mech. **40**, 1–24 (2008).

[125]O. Pouliquen and Y. Forterre, "Friction law for dense granular flows: Application to the motion of a mass down a rough inclined plane," J. Fluid Mech. **453**, 133–151 (2002).

[126]T. M. J. Nijssen, M. A. H. Dijk, H. A. M. Kuipers, J. van der Stel, A. T. Adema, and K. A. Buist, "Experiments on floating bed rotating drums using magnetic particle tracking," AIChE J. **68**, e17627 (2022).

[127]F. Chen and H. Yan, "Elastic–viscoplastic constitutive theory of dense granular flow and its three-dimensional numerical realization," Phys. Fluids **33**, 123310 (2021).

[128]D. A. Santos, M. A. S. Barrozo, C. R. Duarte, F. Weigler, and J. Mellmann, "Investigation of particle dynamics in a rotary drum by means of experiments and numerical simulations using DEM," Adv. Powder Technol. **27**, 692–703 (2016).

[129]P. C. Carman, "Permeability of saturated sands, soils and clays," J. Agric. Sci. **29**, 262–273 (1939).